Strength improvement of CoCrNi medium entropy alloy through introducing lattice defects in refined grains

Jianying Wang[1], Jianpeng Zou[1], Hailin Yang[1,*], Hua Huang[1], Zhilin Liu[2], Shouxun Ji[3]

1. State Key Laboratory of Powder Metallurgy, Central South University, Changsha 410083, China

2. Light Alloy Research Institute, College of Mechanical and Electrical Engineering, Central South University, Changsha, 410083, China

3. Brunel Centre for Advanced Solidification Technology (BCAST), Brunel University London, Uxbridge, Middlesex, UB8 3PH, United Kingdom

* Corresponding authors: y-hailin@csu.edu.cn

Abstract:

Through architecting lattice defects in refined grains, superior mechanical performance of CoCrNi medium entropy alloy can be achieved without adding alloying elements and/or extra particles. Processing routes including a cold rolling with subsequent annealing were applied on the alloy samples prepared by gas atomization and spark plasma sintering (SPS). On top of the refined grains of f.c.c matrix (～2.35 μm), various lattice defects were also introduced after processing, including high density of dislocations, stacking faults (SFs), Lomer-Cottrell locks (LCs) and nanotwins, which could significantly improve the mechanical properties. In particular, the yield strength, ultimate tensile strength, and fracture strain of the alloy reached 1.36 GPa, 1.50 GPa, and 7.3%, respectively, after rolling with 70% thickness reduction and annealing at 600 ºC for 2 h. The significant improvement in strength is mainly attributed to the refined grains, creation of high dislocation density and other lattice defects, resulting from the innovative processing in SPS, severe deformation and the subsequent annealing.

Keywords: Medium-entropy alloys; CoCrNi alloy; Microstructure; Mechanical properties; Lattice defects; Grain refinement

1. Introduction

Medium/High entropy alloys are highly regarded as potential candidates to replace traditional metallic materials owing to their superior mechanical, physical and chemical properties [1–6]. Among the multi-principal element alloys, CoCrNi medium-entropy alloys (MEAs) have exceptional ductility, fracture toughness and excellent corrosion resistance due to the plastic deformation modes (i.e., slips of {111}1/2<110> dislocations and/or twins associated with successive gliding of {111}1/6<112> Shockley partial dislocations [7–9]) and high content of corrosion-resistant elements (Cr and Ni) [10,11]. However, superior ductility and fracture toughness of as-cast/as-sintered CoCrNi alloys are still insufficient in many industrial applications where strength is a pivotal requirement. Therefore, one of the keen demands is to further improve the mechanical properties of CoCrNi alloys.

Taking the nature of simple solid solution of MEAs into account, the improvement in mechanical properties of MEAs through precipitation strengthening and/or forming particle reinforcement is attractive and the progresses have shown the success in a number of systems. For instance, the crystal structures of CoCrNi alloys can be tuned by adding Mo trace element, which facilitates to form the strong lattice distortion and precipitates (σ and μ), leading to the impediment to dislocation movement [12,13]. Moreover, a small amount of Ti and Al additions have been introduced in CoCrNi alloys to increase the nucleation rate of $L1_2$-type of γ/γ' precipitates. The coherent orientation relationship (OR) between f.c.c matrix and γ/γ' precipitates deliver outstanding comprehensive mechanical properties in CoCrNi alloys [14,15]. Additionally, *ex-situ* particles (i.e. B_4C [16] and SiC [17]) have also been employed to enhance mechanical properties of CoCrNi alloys. Regrettably, most of the reinforcement particles often improve the strength, but impair the ductility in CoCrNi alloys. Actually, the increase in alloying elements or *ex-situ* particles makes materials more resource dependent and the recycling and reuse of materials become relatively difficult to meet sustainability requirement. Therefore, it desires effective strategies in materials processing for improving the mechanical performance of MEAs.

Previous studies have indicated that introducing fine grain and tailoring lattice defect are practically achievable to develop high-performance alloys with superior mechanical properties [18–21]. For example, the reduction in the grain sizes of CoCrFeMnNi HEA from 155 to 4.5 mm resulted in a dramatic increase in the yield strength from 170 to 360 MPa [18]. Similarly, Ganji et al. [19] investigated the mechanical properties of AlCoCrCuFeNi HEA with average grain sizes between 112 and 1550 nm. The AlCoCrCuFeNi HEA with fine grains presented very high yield strength [19]. Additionally, for MEAs/HEAs with low SFE,

the most commonly observed lattice defects, i.e. dislocations, SFs and nanotwins, also tend to form readily during materials processing or mechanical deformation [22–26]. For instance, based on the low SFE of {111} plane of 3.5 mJ/m^2, SFs, nano-twins, hcp phase, LCs and amorphous bands can be introduced into a nano-structured $Cr_{26}Mn_{20}Fe_{20}Co_{20}Ni_{14}$ alloy under the condition of tensile test at a lower temperature of -180 °C. The evolution of these lattice defects at different strain levels provided strong barriers and delivered the improvement in mechanical properties [24]. Additionally, the CoCrFeNi alloy enhanced the formation of nanotwin boundaries, and then blocked the dislocation glide during straining, which brought a promising strength/elongation of 1.2 GPa/13.6% [26]. On the other hand, a combination method of gas atomization and spark plasma sintering (SPS) offer significant advantages such as processing efficiency, less risk of contamination, modification of segregation, and grain refinement [27,28]. Particularly, the refined microstructure of MEAs/HEAs introduced by SPS contributed to improve hardness and strength in comparison with traditional casting method [7,12]. Thus, through architecting the fine grains and defect structures across different length scales, novel mechanical performance can be possibly developed in the "plain" materials without adding other chemical alloying elements or *ex-situ* particles.

In this work, based on the characteristics of rapid sintering of SPS and low SFE of the CoCrNi alloy, we aim to explore the capability of processing routes that introduce fine grains and various lattice defects. Cold deformation and subsequent annealing are applied on the pure CoCrNi alloy samples made by gas atomization (GA) and SPS. Meanwhile, the optimum process to achieve excellent mechanical properties CoCrNi alloys is studied for the microstructural evolution and mechanical behaviour during processing. The discussion focuses on the dominant mechanisms responsible for strengthening.

2. Experimental

2.1 Materials and processing

The CoCrNi alloy powder was fabricated by the gas atomization using high-pressure N_2. The average size of CoCrNi powder used in this work was approximately 34.6 μm. Inductively coupled plasma atomic emission spectrometry (ICAP 7000 Series) was applied to characterize the powder chemical composition, as shown in Table 1. Sintering was performed by compacting the CoCrNi powder in a graphite die, followed by spark plasma sintering (SPS). The sintering temperature, heating rate, pressure and holding time were 1130 °C, 100 °C/min, 40 MPa and 15 min, respectively. In addition, a coating layer of cubic boron nitride was sprayed on the inner surface of the graphite sheet as a thermal barrier layer to prevent the diffusion of carbon during sintering. The SPSed alloy samples were then sliced to

10 mm thick strips and subsequently rolled by 50% and 70% reduction in thickness at room temperature. Afterwards, the as-rolled samples were annealed individually in an electric resistance furnace at a temperature from 600 °C to 900 °C, followed by water quenching. The whole experimental procedures are schematically shown in Fig. 1.

Table 1. Chemical Compositions of the CoCrNi pre-alloyed powder (wt.%).

Element	Co	Cr	Ni	Fe	C	O	N	P	S
wt.%	34.9	30.4	34.5	0.063	0.0036	0.0015	0.0021	0.0012	0.00034

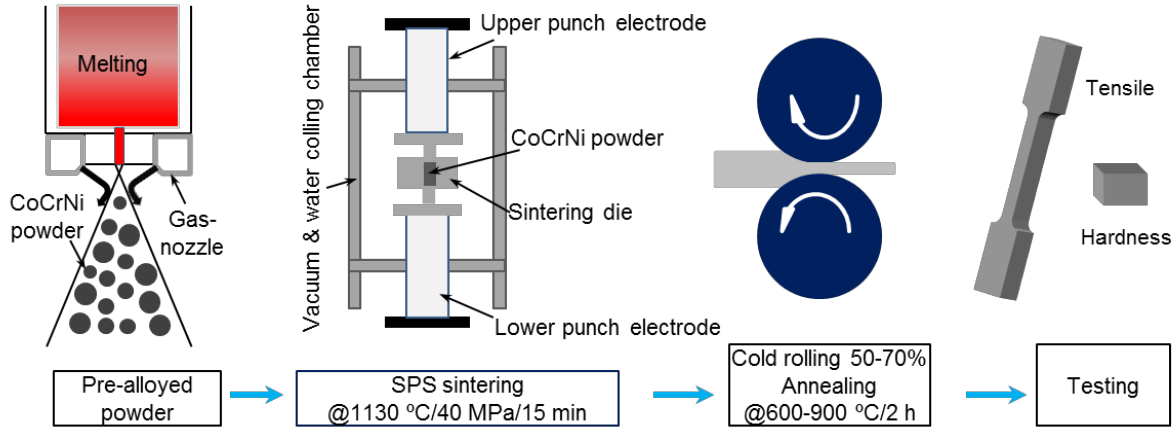

Fig. 1. Schematic diagram showing the experimental procedures of the CoCrNi alloy from powder preparation, SPS sintering, rolling, annealing, to tensile testing.

2.2 Microstructural characterization

The crystal structures of the CoCrNi alloy under different conditions were examined by X-ray diffraction technique with Cu *K*a radiation (XRD, Rigaku). Microstructure features of the alloy were characterized using electron microscopes. Scanning electron microscope (SEM), backscattered electron microscope (BSE) and electron backscatter diffraction (EBSD) orientation mappings were conducted in a FIB Helios NanoLab G3 UC system equipped with a Hikari camera and the TSL OIM data analysis software for EBSD. Before SEM/BSE, EBSD and XRD characterization, the samples were firstly ground with SiC papers diamond suspensions and then polished using 40 nm colloidal silica suspension. The detailed microstructures were examined by transmission electron microscope (TEM; Titan G2 60-300). The mechanically-polished TEM samples were refined using the precision ion polishing system (PIPS) at a voltage of 5 kV/2 kV and an incident angle of 3º ~ 7º.

2.3 Mechanical properties

The dog-bone-shaped tensile samples with a gauge length of 22 mm and cross-section of 2.2 × 1.5 mm^2 were fabricated using electrical discharge machining. A MTS Alliance RT30 mechanical testing system was used to evaluate uniaxial tensile properties at a strain rate of 1×10^{-3} s^{-1} at room temperature (25 ºC). Meanwhile, cubic samples with a dimension of 10 × 10 × 1.5 mm^3 were prepared for hardness measurement. The micro-hardness was measured using a Vickers hardness testing machine (600 HVS-1000AVT) with a loading force of 100 g and a dwelling time of 15 s. To eliminate the measurement errors, five to eight tests were conducted, and the average value was considered as final result.

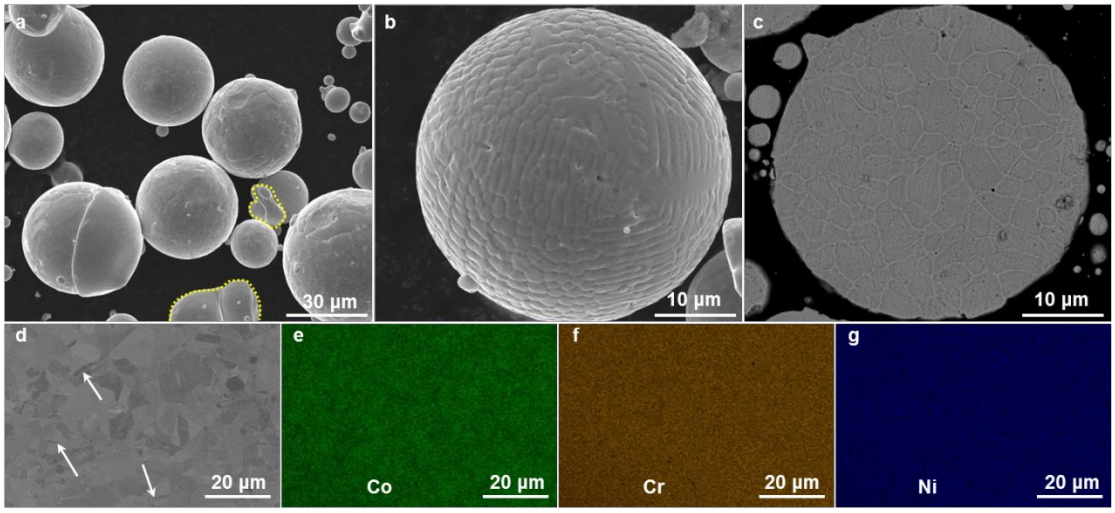

Fig. 2. SEM micrographs showing (a, b) the surfaces and (c) cross-sectioned morphology of CoCrNi gas-atomized powder particle; (d) SEM/BSE image showing the microstructure of the CoCrNi alloy after sintering; (e-g) EDS mapping showing the elemental distribution of the CoCrNi alloy after sintering. The white arrows in (d) indicate the occurrence of annealing twins.

3. Results

3.1 Microstructural feature

Figs. 2a-b show SEM micrographs of the gas atomized CoCrNi powder. The majority of raw gas-atomized powder particles showed spherical morphology. Several particles were observed with the attachment of fine satellites and very few particles were relatively flat with rounded edges (marked by the yellow circles in Fig. 2a). The formation of abnormal particles mainly originated from the materials preparation processing, where the spheroidization time of liquid droplets was longer than solidification time. Thus, the pre-alloyed powder completed solidification before final spheroidization. Also, the surface morphologies and cross-sectional microstructure of powder particles in Figs. 2b and 2c revealed the existence of visible dendrite arms and fine equiaxed structures with a size of 2 ~ 10 μm. Moreover, the

microstructure (Fig. 2d) displayed a homogeneous single phase with a number of annealing twins in the as-SPSed alloy. EDS elemental mapping of the alloy in Figs. 2e-g confirmed that all the elements were dispersed uniformly in the matrix.

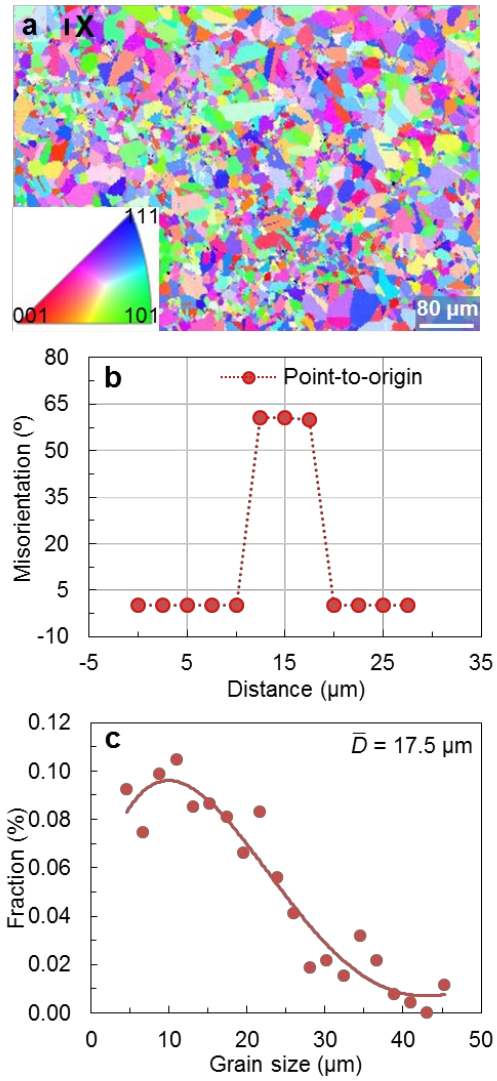

Fig. 3. (a) EBSD orientation mapping image showing the grain structures of the as-SPSed CoCrNi alloy; (b) misorientation degrees along the black line X in (a) identifying representative annealing twins; and (c) distributions of grain sizes in the as-SPSed CoCrNi alloy.

Fig. 3 represents the EBSD analysis for the microstructure of the as-SPSed CoCrNi alloy. Similar to the results of SEM/BSE, the equiaxed or nearly-equiaxed grains were observed in Fig. 3a. Annealing twins were also characterized along the black line X in Fig. 3a, as confirmed by the 60º misorientation degree in Fig. 3b. The distribution of grain sizes is shown in Fig. 3c. It can be seen that the average grain size (17.5 μm) of f.c.c matrix (without considering annealing twins) was smaller than that of pre-alloyed powder. This can be attributed to two aspects: (i) the larger surface of powder particles has more than one nucleation sites for solidification, as indicated in Fig. 2c; and (ii) the SPS process can inhibit

grain growth during sintering because of the quick heating and cooling.

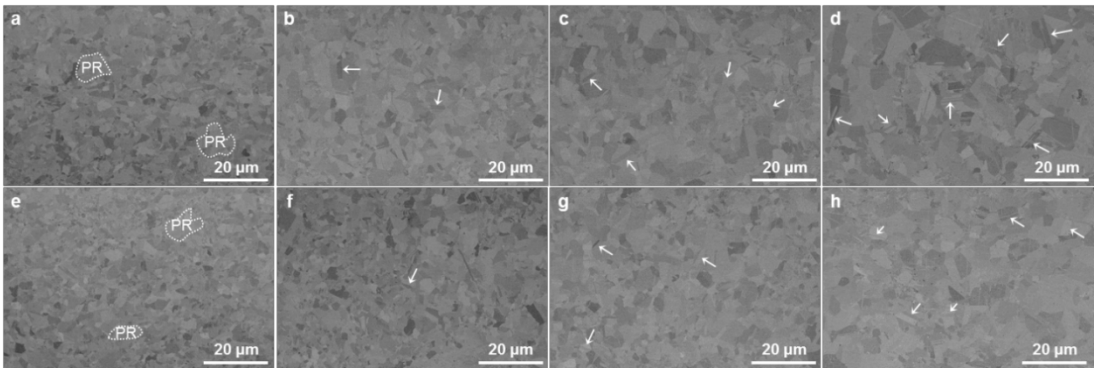

Fig. 4. SEM/BSE micrographs showing the microstructure of the CoCrNi alloy with different reduction thicknesses and annealing conditions; (a) 50% thickness reduction and annealing at 600 ºC / 2 h; (b) 50% thickness reduction and annealing at 700 ºC / 2 h; (c) 50% thickness reduction and annealing at 800 ºC / 2 h; (d) 50% thickness reduction and annealing at 900 ºC / 2 h; (e) 70% thickness reduction and annealing at 600 ºC / 2 h; (f) 70% thickness reduction and annealing at 700 ºC / 2 h; (g) 70% thickness reduction and annealing at 800 ºC / 2 h; (h) 70% thickness reduction and annealing at 900 ºC / 2 h. The white arrows indicate the formation of annealing twins, and PR represents the partially recrystallized grains.

The microstructures obtained by SEM/BSE for the CoCrNi alloy with different reduction thicknesses and annealing conditions are shown in Fig. 4. Obviously, the heterogeneous microstructure was featured by the mixture of partially recrystallized grains and fully recrystallized (FR) grains in the samples processed with 50% and 70% thickness reductions and annealing at 600 ºC for 2 h, as shown in Figs. 4a and 4e. As the annealing temperature increased from 700 ºC to 900 ºC, the microstructure was completely transformed into FR grains with submicron twins. Moreover, the density of annealing twins and the average grain size of f.c.c matrix increased with increasing the annealing temperatures.

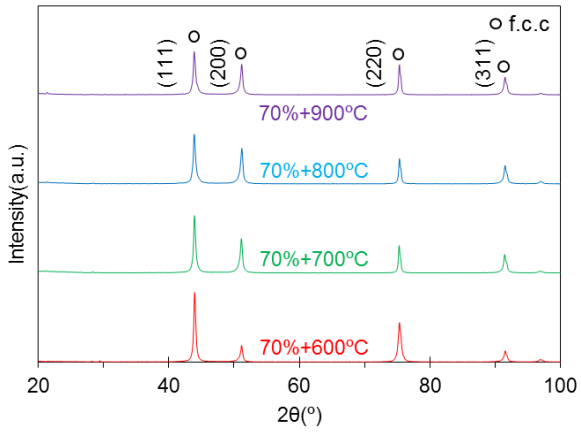

Fig. 5. XRD spectra of the CoCrNi alloy after cold rolling with 70% thickness reduction and annealing at 600 ºC - 900 ºC.

Fig. 5 shows the XRD results of the CoCrNi alloy processed by 70% thickness reduction and

annealing at 600 ºC - 900 ºC. The signal peaks of f.c.c phase occurred in all samples. The high intensity of the (111) peak relative to others indicated the existence of a relatively preferred orientation of the sample annealed at 600 ºC. Such a preferred orientation decayed with increasing annealing temperatures.

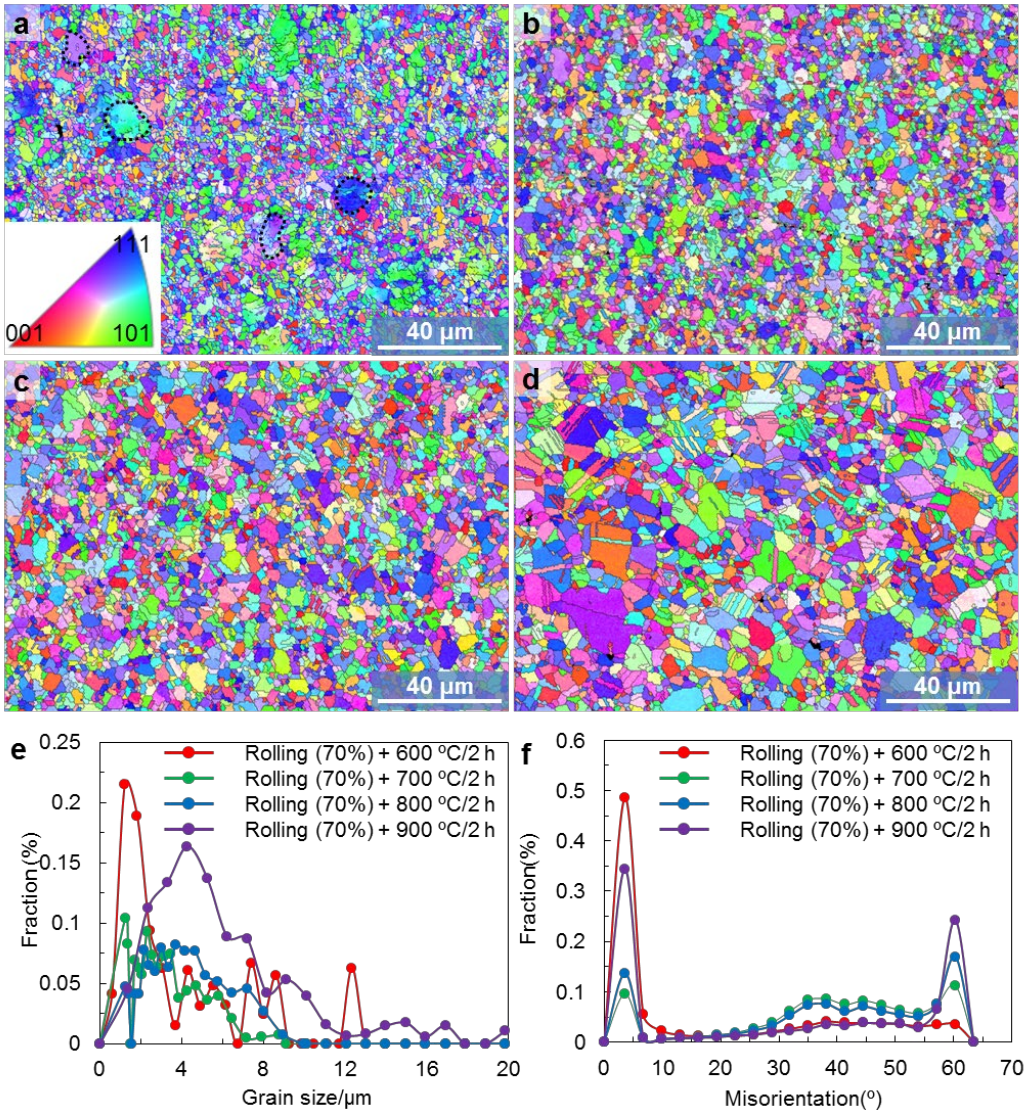

Fig. 6. (a-d) EBSD mapping (Inverse Pole Figure (IPF); (e) distributions of grain sizes and (f) distributions of misorientation angles in the alloy after 70% thickness reduction and annealing at 600 ºC - 900 ºC. The black dash circles in (a) represent the partially recrystallized grains.

The grain orientation, average grain size and misorientation of the CoCrNi alloy after being processed by 70% thickness reduction and annealing at 600 ºC - 900 ºC were studied using EBSD to further unravel the effect of annealing temperature on the microstructural evolution. The IPF maps, grain size distributions and misorientation angle distributions are shown in Fig. 6. Similar to the results in Fig. 4e, the microstructure of CoCrNi alloy rolled by 70% thickness reduction and annealed at 600 ºC consisted of the partially recrystallized grains (the black dash circle in Fig. 6) and FR grains with the average grain size of 2.35 μm. Obviously,

small grain sizes introduced by SPS and severe deformation provided a solid basis for superior mechanical behaviour. As the annealing temperature increased, the FR equiaxed grains were obviously increased. The average grain sizes were 2.93 μm, 3.81 μm and 6.03 μm for the alloys annealed at 700 ºC, 800 ºC and 900 ºC, respectively. Meanwhile, the misorientation angles appeared evidently at 60°, indicating that the number density of annealing twins was increased. Furthermore, annealing at lower temperatures increased the density of low-angle grain boundaries (LAGBs) with misorientation < 15° (Fig. 6f). LAGBs have been identified along with the well-organized arrays of individual dislocation [29] and can significantly affect the associated mechanical properties.

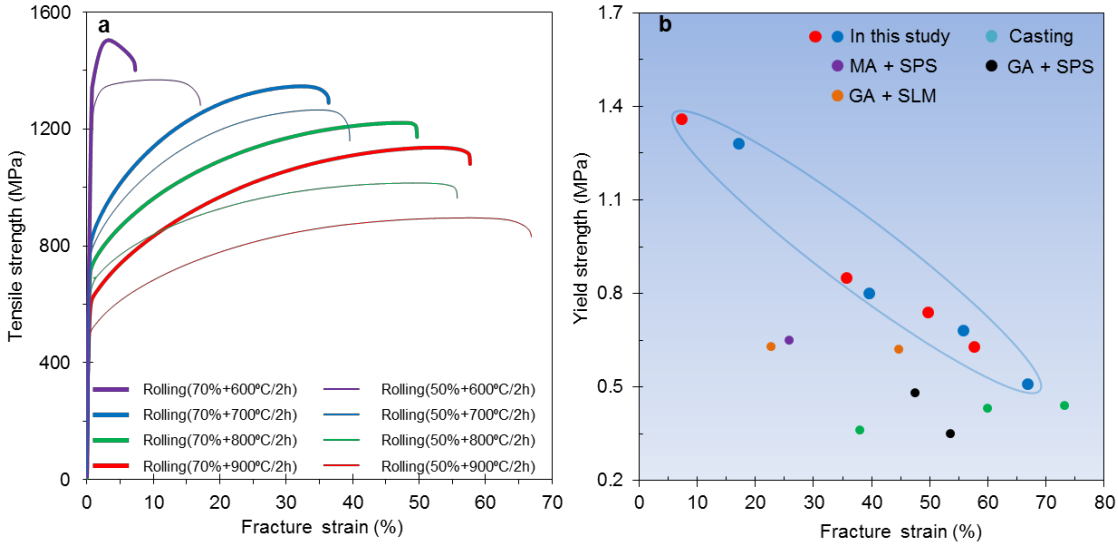

Fig. 7. Tensile stress-strain curves of the CoCrNi alloy under different processing conditions at room temperature; (b) comparison of tensile properties of CoCrNi alloys fabricated between in this work and other methods, including casting [8,14,30], mechanical alloying (MA) + SPS [31], gas atomization (GA) + SPS [3,7] and gas atomization (GA) + selective laser melting (SLM) [32,33].

3.2 Mechanical properties

Tensile stress-strain curves of the CoCrNi alloy under different processing conditions are shown in Fig. 7, and the corresponding data for tension and hardness are summarized in Table 2. Our previous study [3] has confirmed that the as-SPSed CoCrNi alloy can offer the yield strength of 0.35 GPa, ultimate tensile strength (UTS) of 0.80 GPa, Vickers hardness of 195.0 Hv, and fracture strain of 53.6%. Clearly, the remarkable response can be seen from the results in Fig. 7. After cold rolling with 50% thickness reduction and annealing at 600 ºC, the yield strength and the fracture strain were increased to 1.28 GPa and 17.1%, respectively. Meanwhile, the annealing temperature also significantly affected mechanical performance. The yield strength and fracture strain were 0.80 GPa and 39.6% for the alloy annealed at 700 ºC / 2 h, 0.68 GPa and 55.8% for the alloy annealed at 800 ºC / 2 h, 0.51 GPa and 66.9% for

the alloy annealed at 900 ºC / 2 h. Moreover, the increasing deformation severity resulted in the significant improvement in strength with a scarification of fracture strain. The samples obtained after cold rolling with 70% thickness reduction delivered higher tensile strengths and lower fracture strains in comparison with that were obtained from the cold rolling with 50% thickness reduction. The yield strength and UTS reached the peak values of 1.36 GPa and 1.50 GPa after cold rolling with 70% thickness reduction and annealing at 600 ºC / 2 h. Also, Fig. 7(b) shows a comparison of tensile data of the CoCrNi alloy fabricated between in this work and other methods, including casting [8,14,30], mechanical alloying (MA) + SPS [31], gas atomization (GA) + SPS [3,7] and gas atomization (GA) + selective laser melting (SLM) [32,33]. Obviously, the alloy fabricated in the present work exhibited better comprehensive mechanical properties than the CoCrNi alloys fabricated by other methods.

Table 2. The yield strength (YS), ultimate tensile strength (UTS), fracture strain (FS), and Vickers hardness for the CoCrNi alloy under different processing conditions.

Treatment	YS (GPa)	UTS (GPa)	FS (%)	Hardness (Hv)
As-SPSed CoCrNi [3]	0.35	0.80	53.6	195.0
Rolled at 50% and annealed at 600 ºC/2 hrs	1.28	1.36	17.1	410.6
Rolled at 50% and annealed at 700 ºC/2 hrs	0.80	1.26	39.6	283.5
Rolled at 50% and annealed at 800 ºC/2 hrs	0.68	1.02	55.8	257.1
Rolled at 50% and annealed at 900 ºC/2 hrs	0.51	0.89	66.9	250.3
Rolled at 70% and annealed at 600 ºC/2 hrs	1.36	1.50	7.3	450.2
Rolled at 70% and annealed at 700 ºC/2 hrs	0.85	1.34	35.7	370.9
Rolled at 70% and annealed at 800 ºC/2 hrs	0.74	1.22	49.7	295.8
Rolled at 70% and annealed at 900 ºC/2 hrs	0.63	1.13	57.7	281.4

4. Discussion

4.1 Strengthening mechanisms

The CoCrNi alloy treated by cold rolling and annealing can deliver a significant improvement in mechanical properties. Particularly, the CoCrNi alloy exhibits the yield strength of 1.36 GPa, UTS of 1.50 GPa and fracture strain of 7.3% after cold rolling with 70% thickness reduction and annealing at 600 ºC / 2 h. Since there is no precipitation strengthening and solid solution strengthening induced by the introduction of elements with large atomic sizes, the high strength is mainly attributed to the combined effect of multiple strengthening mechanisms of fine grain strengthening (σ_g) and dislocation strengthening (σ_{dis}). Therefore, the contribution of the mainly strengthening mechanisms of the alloy can be expressed as:

$$\sigma_y = \sigma_g + \sigma_{dis} \quad [1]$$

The part of strengthening effects by grain refinement (σ_g) can be calculated via the Hall-Petch relationship, as the following formula [34]:

$$\sigma_g = K(d^{-0.5} - d_0^{0.5}) \quad [2]$$

where K is a constant (265 MPa•μm$^{1/2}$ for CoCrNi alloy [35]). From the Fig. 3a and Fig. 6a, the average grain size of CoCrNi alloy under the conditions of as-SPSed and rolling with 70% thickness reduction and annealing at 600 ºC / 2 h are 17.5 μm and 2.35 μm, respectively. As a consequent, the strength contribution from grain refinement to yield strength is evaluated as 109.5 MPa.

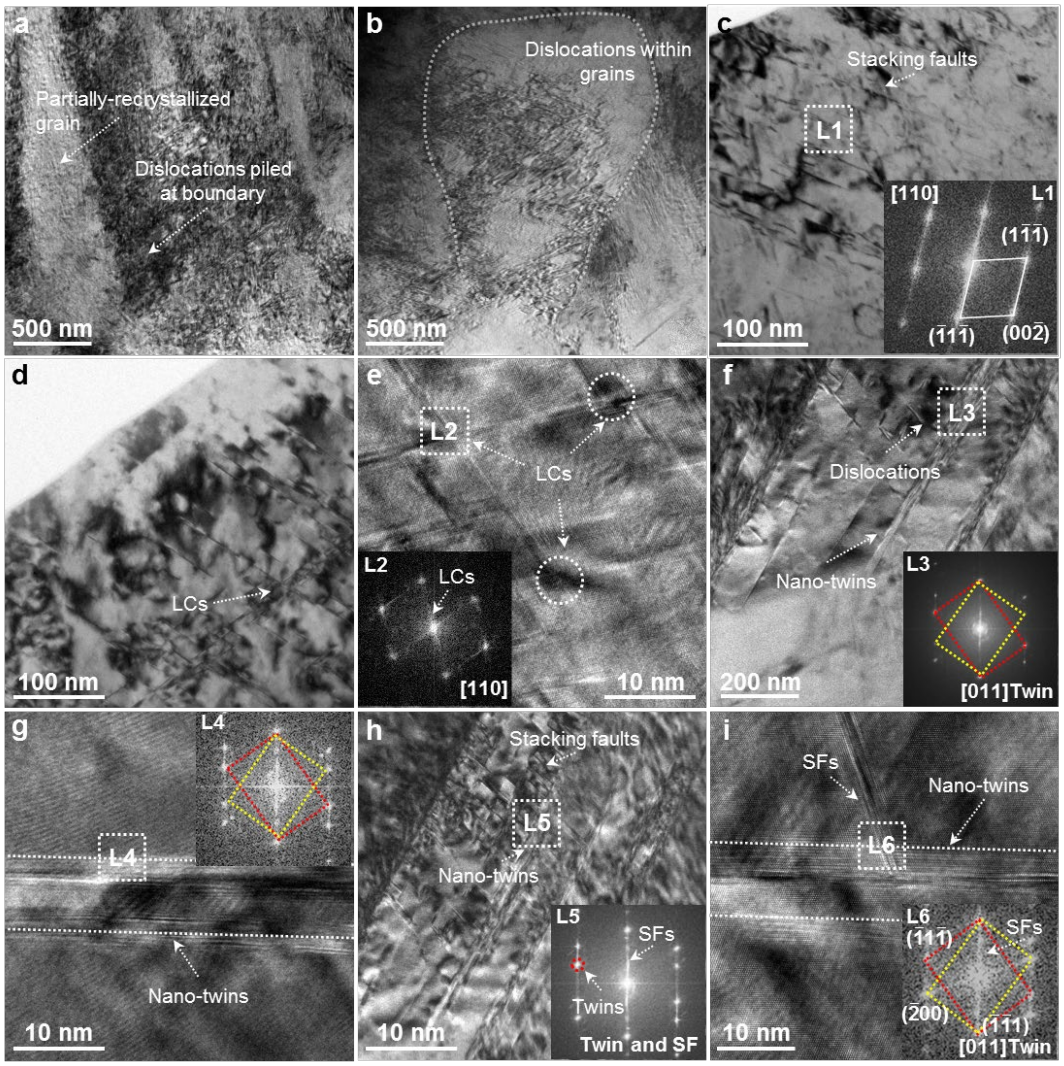

Fig. 8. TEM micrographs of the CoCrNi alloy with 70% thickness reduction and 600 ºC / 2 h, showing (a,b) the formation of high number density dislocations; the bright-field TEM image collected from specific areas (c) with stacking faults and (d) Lomer-Cottrell locks (LCs); (e) high-resolution TEM shows the formation of Lomer-Cottrell locks (LCs); (f) dislocations piled up at nano-twins; (g) high-resolution TEM exhibiting the formation of nano-twins; (h) the bright-field TEM image and (i) high-resolution TEM showing the interaction between stacking faults and nano-twins.

Apart from the obvious fine grain strengthening induced by SPS and severe deformation,

higher number density of dislocations piling up at grain boundaries can be also observed in the bright-field TEM image of Fig. 8a. The contribution of σ_{dis} can be estimated according to Taylor's hardening law:

$$\sigma_{dis} = M \bullet \alpha \bullet G \bullet b \bullet \rho^{0.5} \quad [3]$$

where M, a, G, b, and ρ are the Taylor factor, empirical constant, shear modulus, Burgers vector, and dislocation density. For CoCrNi alloy, the above parameters are: M = 3.06 [36]; a = 0.2 [36]; G = 85 GPa [12]; b = 0.253 nm [14]. Generally, the total dislocation density is composed of geometrically necessary dislocation (GND) and statistical storage dislocation (SSD). GND is cause by uniform deformation. It is mainly distributed in the grain boundary region and the restricted boundary region and the restricted boundary region, while the SSD is mainly distributed inside the grain, and therefore the main contribution of dislocation enhancement comes from the GND. According to Eq. [3] proceed Kubin et al., the kernel average misorientation (KAM) map was used to calculate GND by combining local strain [37]:

$$\rho_{GND} = 2\vartheta/(\mu b) \quad [4]$$

where ϑ is the average value of KAM (1.30), μ is the step size (4.0 μm) during EBSD measurement, and b is the Burger vector (0.253 nm [14]). Correspondingly, the ρ_{GND} was estimated to be ~ 2.57 × 10^{15} m^{-2}, and the contribution of dislocation density is about 654.1 MPa. The estimated yield strength (as-SPSed (352.0 MPa) + σ_g (109.5 MPa) +σ_{dis} (654.1)) is ~1.12 GPa, which is lower than the measured yield strength of 1.36 GPa. Therefore, the high yield strength of CoCrNi alloy also originates from some other factors. In this work, besides high density of dislocations, we also observed other lattice defects. For instance, higher number density of SFs nucleated and grown from the matrix is also observed in Fig. 8c. In Fig. 8d and 8e, the SFs also move and intersect to form Lomer-Cottrell locks (LCs). With the high number density of SFs and LCs produced within a band-like structure, the dislocation transmission is hindered by SFs and LCs on the conjugate plane (Figs. 8c and 8d). Moreover, the nanotwins are characterized by bright-field image and SAED pattern of L3 (Fig. 8f). It is anticipated that some nanotwins have not experienced sufficient growth when annealing is at 600 °C for 2 h. The thickness of these nanotwins spans from a few to tens of nanometres (Fig. 8g). Furthermore, the interactions between nanotwins and SFs are shown in Figs. 8h and 8i. Previous studies have confirmed that, in low SFE f.c.c alloys, slips are arrested at grain boundaries. With increasing the applied stress, the number of dislocations pileups increases to achieve a critical stress, above which slip is transmitted across the boundaries [38–40]. Schematically, a representative 3D microstructure of the CoCrNi alloy with low SFE that contains principal constituents is constructed in Fig. 9. The improved strength is not only

induced by obvious grain refinement, SFs, LCs, nano-twins, and interface between SFs and annealing twins can also provide boundaries to inhibit the movement of high number density of dislocations and improve the yield strength further.

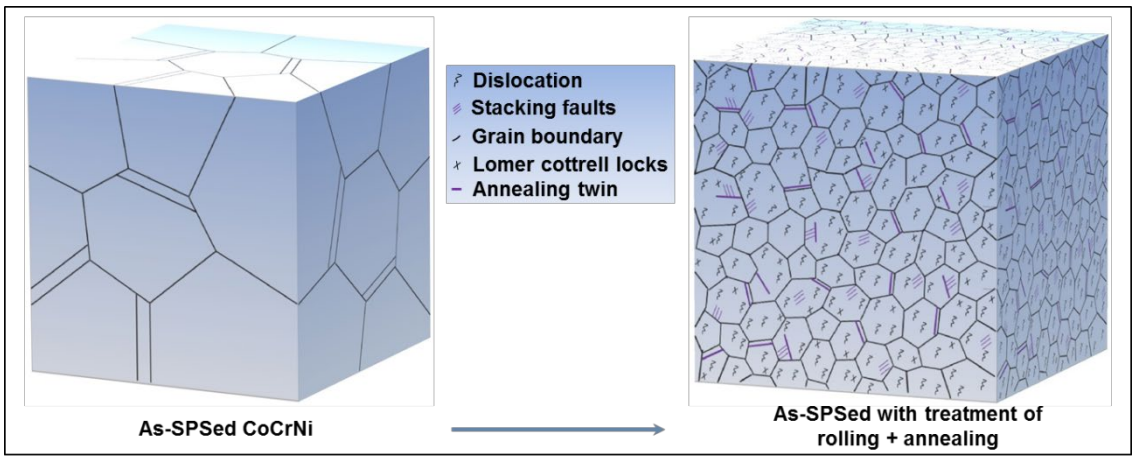

Fig. 9. Diagram showing the three-dimensional (3D) structure in the CoCrNi alloy, showing different major strengthening components, including grain refinement, dislocations and other lattice defects.

4.2 The influence of rolling reduction and annealing temperature on mechanical properties

The Vickers hardness of the CoCrNi alloy under different conditions is shown in Fig. 10. Three zones can be seen for the as-SPSed alloy, rolled alloy with 50% thickness reduction and rolled alloy with 70% thickness reduction. For the alloy with rolling and annealing, the hardness increases initially with increasing the annealing temperatures to achieve the peak and then decreases with increasing the annealing temperatures. The peak hardness is 425.3 Hv at 550 ºC and 450.2 Hv at 600 ºC for the alloy with 50 % and 70% thickness reduction and annealing.

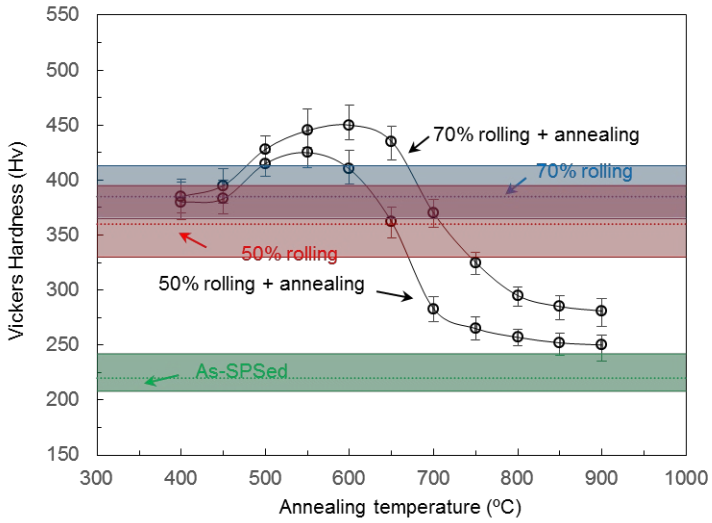

Fig. 10. Vickers hardness of the CrCoNi alloy under different conditions. All the annealing time is 2 h.

Definitely, annealing at 550 ºC and 600 ºC leads to the decrease in defect density [41]. In this work, as shown in Fig. 4e and Fig 8a, the low temperature annealing resulted in the mixture of recrystallized grains. Because the dislocations are only partially relaxed, the dislocations within grains will migrate to boundaries during annealing, resulting in the enhancement in density of dislocations at boundaries of partially recrystallized grains. And, therefore, lattice defects in grain boundaries increased (Fig. 8a). The high-density dislocations accumulate at the grain boundaries and entangle each other to dynamically suppress grain slip. This is the main possible reason for the increase in hardness. In addition, the previous study [30] has suggested that the hardness of the CoCrNi alloy after annealing at 600 °C for 4 h is approximately equal to the value obtained by annealing at 700 °C for 1 h. Thus, low annealing temperature can retain more lattice defects introduced by rolling and deliver high strength. Furthermore, the IPF and kernel average misorientation (KAM) of the CoCrNi alloy processed by cold rolling with 50% thickness reduction and annealing at 600 °C are shown in Fig. 11. It is seen that the average grain size is 2.96 μm, which is coarser than that of 2.35 μm obtained from the alloy processed by cold rolling with 70% thickness reduction and annealing at 600 °C. Obviously, finer grain sizes can offer higher volume fractions of grain boundaries, which can offer more impedance for dislocation motion.

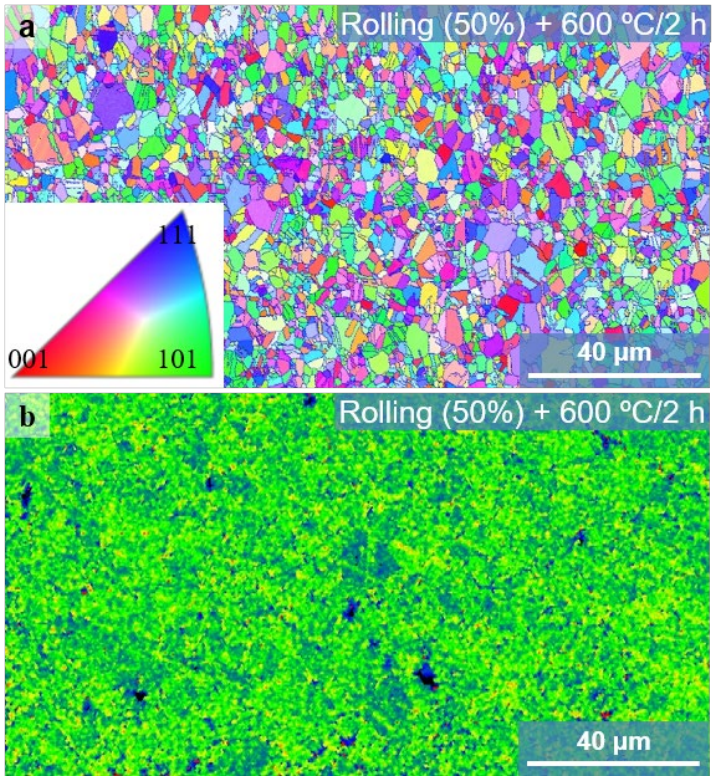

Fig. 11. (a) EBSD mapping with the insert of Inverse Pole Figure (IPF) and (b) Kernel Average Misorientation (KAM) of the CoCrNi alloys after cold rolling with 50% thickness reduction and annealing at 600 ºC for 2 h.

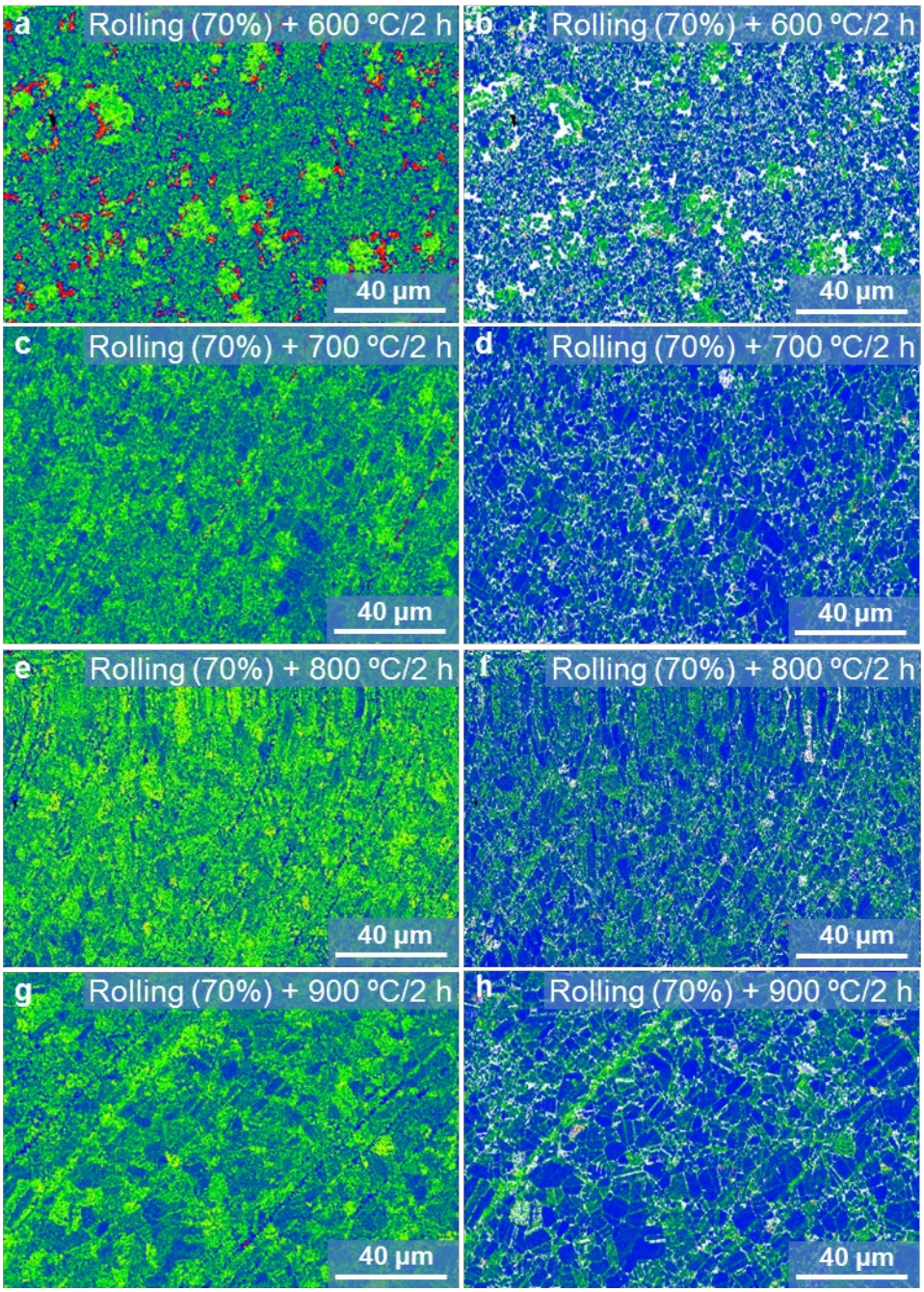

Fig. 12. (a,c,e,g) Kernel Average Misorientation (KAM) and (b,d,f,h) geometrically necessary dislocations (GNDs) maps of the CoCrNi alloys after cold rolling with 70% reduction followed by different annealing treatments; (a,b) 600 ºC / 2 h; (c,d) 700 ºC / 2 h; (e,f) 800 ºC / 2 h; (g,h) 900 ºC / 2 h.

Moreover, Fig. 12 presents the KAM images and GND maps of the CoCrNi alloy processed by cold rolling with 70% thickness reduction and annealing at 600 °C - 900 °C. The variations in average KAM with increasing temperature qualitatively reflect the degree of plastic deformation or defect density [42]. The average KAM of the CoCrNi alloy rolled with 70% thickness reduction and annealed at 600 ºC is 1.30, which is high due to the accumulation of strain energy inside the alloy and the multiplication of dislocations.

Meanwhile, additional stress is introduced into the boundaries of adjacent grains to guarantee strain compatibility during plastic deformation, which increases the number density of GNDs [43]. As shown in Eq. [3], the density of GNDs has a positive correlation with the KAM. Therefore, as the annealing temperature increases, the average KAM decreases sharply. The continuous dynamic recovery and recrystallization decrease the density of GNDs. Consequently, when the annealing temperature increased up to 900 ºC, the average value of KAM (0.86) decreases obviously. Also, the average KAM of the CoCrNi alloy with 50% thickness reduction and annealing at 600 ºC is 1.15, which is lower than that of the alloy with 70% thickness reduction and 600 ºC annealing temperature (1.30). This indicates that the higher number density of GNDs can be introduced by severe deformation. As a result, the finer grain sizes and the high density of GNDs deliver a significant improvement in the strength of the CoCrNi alloy with higher reduction thickness.

5. Conclusions

(1) Architecting fine grain structures with different lattice defects by tailoring the treatment of deformation and annealing, superior mechanical performance can be achieved in the CoCrNi alloy obtained by SPS sintering of powders.

(2) The CoCrNi alloy after cold rolling with 70% thickness reduction and annealing at 600 ºC for 2 h offers a remarkable strengthening, in which the yield strength of 1.36 GPa, ultimate tensile strength of 1.50 GPa, hardness of 450.2 Hv, and fracture strain of 7.3% can be achievable. The fine grains of f.c.c matrix (～2.35 μm), dislocation strengthening and various other lattice defects (i.e., SFs, LCs and nanotwins) contribute to the improvement in strength.

(3) The severe deformation from cold rolling can offer improved yield strength with a scarification of fracture strain. The higher annealing temperature can promote the improvement in ductility.

Acknowledgments

Financial support from the National Key Research and Development Program of China (grant number 2020YFB0311300ZL) is greatly acknowledged. Financial support from National Natural Science Foundation of China (No. 52071343) is also greatly acknowledged.

Data availability

The raw/processed data required to reproduce these findings cannot be shared at this time as the data also forms part of an ongoing study.

Declaration of Competing Interest

All authors declare that they have no known competing financial interests or personal relationships that could have appeared to influence the work reported in this paper.

References

[1] J.W. Yeh, S.K. Chen, S.J. Lin, J.Y. Gan, T.S. Chin, T.T. Shun, C.H. Tsau, S.Y. Chang, Nanostructured high-entropy alloys with multiple principal elements: novel alloy design concepts and outcomes, Adv. Eng. Mater. 6 (2004) 299–303.

[2] B. Cantor, I.T.H. Chang, P. Knight, A.J.B. Vincent, Microstructural development in equiatomic multicomponent alloys, Mater. Sci. Eng. A 375–377 (2004) 213–218.

[3] J.Y. Wang, H.L. Yang, J.M. Ruan, Y. Wang, S. Ji, Microstructure and properties of CoCrNi medium-entropy alloy produced by gas atomization and spark plasma sintering, J. Mater. Res. 34 (12) (2019) 1–11.

[4] X. Lu, D. Wang, Z.M. Li, Y. Deng, A. Barnoush, Hydrogen susceptibility of an interstitial equimolar high-entropy alloy revealed by *in-situ* electrochemical microcantilever bending test, Mater. Sci. Eng. A 762 (2019) 138114.

[5] J. Xu, X. Kong, M.H. Chen, Q.C. Wang, F.H. Wang, High-entropy FeNiCoCr alloys with improved mechanical and tribological properties by tailoring composition and controlling oxidation, J. Mater. Sci. Technol. 82 (2021) 207–213.

[6] Y. Zhang, T.T. Zuo, Z. Tang, M.C. Gao, K.A. Dahmen, P.K. Liaw, Z.P. Lu, Microstructures and properties of high-entropy alloys, Prog. Mater. Sci. 61 (2014) 1–93.

[7] H. Huang, J.Y. Wang, H.L. Yang, S. Ji, H.L. Yu, Z.L. Liu, Strengthening CoCrNi medium-entropy alloy by tuning lattice defects, Scripta. Mater. 188 (2020) 216–221.

[8] B. Gludovatz, A. Hohenwarter, K.V.S. Thurston, H.B. Bei, Z.G. Wu, E.P. George, R.O. Ritchie, Exceptional damage-tolerance of a medium-entropy alloy CrCoNi at cryogenic temperatures, Nat. Commun. 7 (2016) 10602–10609.

[9] Z.J. Zhang, H.W. Sheng, Z.J. Wang, B. Gludovatz, Z. Zhang, E.P. George, Q. Yu, S.X. Mao, R.O. Ritchie, Dislocation mechanisms and 3D twin architectures generate exceptional strength-ductility-toughness combination in CrCoNi medium-entropy alloy, Nat. Commun. 8 (2017) 14390.

[10] J.Y. Wang, W.H. Li, H.L. Yang, H. Huang, S. Ji, J.M. Ruan, Z.L. Liu, Corrosion behavior of CoCrNi medium-entropy alloy compared with 304 stainless steel in H_2SO_4 and NaOH solutions, Corro. Sci. 177 (2020) 108973.

[11] I. Moravcik, N.S. Peighambardoust, A. Motallebzadeh, L. Moravcikova-Gouvea, C. Liu, J.M. Prabhakar, I. Dlouhy, Z.M. Li, Interstitial nitrogen enhances corrosion resistance of an

equiatomic CoCrNi medium-entropy alloy in sulfuric acid solution, Mater. Charact. 172 (2021) 110869.
[12] J.Y. Wang, H.L. Yang, H. Huang, J.M. Ruan, S. Ji, *In-situ* Mo nanoparticles strengthened CoCrNi medium entropy alloy, J. Alloys. Compd. 798 (2019) 576–586.
[13] W.H. Liu, Z.P. Lu, J.Y. He, J.H. Luan, Z.J. Wang, B. Liu, Y. Liu, M.W. Chen, C.T. Liu, Ductile $CoCrFeNiMo_x$ high entropy alloys strengthened by hard intermetallic phases, Acta Mater. 116 (2016) 332–342.
[14] Y.L. Zhao, T. Yang, Y. Tong, J. Wang, J.H. Luan, Z.B. Jiao, D. Chen, Y. Yang, A. Hu, C.T. Liu, J.J. Kai, Heterogeneous precipitation behaviour and stacking-fault-mediated deformation in a CoCrNi-based medium-entropy alloy, Acta Mater. 138 (2017) 72–82.
[15] N. An, Y. Sun, Y.D. Wu, J.J. Tian, Z.R. Li, Q. Li, J.Y. Chen, X.D. Hui, High temperature strengthening via nanoscale precipitation in wrought CoCrNi-based medium-entropy alloys, Mater. Sci. Eng. A 798 (2020) 140213.
[16] I. Moravick, L. Gouvea, J. Cupera, I. Dlouhy, Preparation and properties of medium entropy CoCrNi/boride metal matrix composite, J. Alloys Compd. 5 (2018) 979–988.
[17] J.Y. Wang, H.L. Yang, H. Huang, J.M. Ruan, S. Ji, Microstructure and mechanical properties of SiC whisker reinforced CoCrNi medium entropy alloys, Mater. Lett. 254 (2019) 77–80.
[18] F. Otto, A. Dlouhý, Ch Somsen, H. Bei, G. Eggeler, E.P. George, The influences of temperature and microstructure on the tensile properties of a CoCrFeMnNi high-entropy alloy, Acta Mater. 61 (15) (2013) 5743–5755.
[19] R. SreeGanji, P. Sai Karthik, K. Bhanu Sankara Rao, K.V. Rajulapati, Strengthening mechanisms in equiatomic ultrafine grained AlCoCrCuFeNi high-entropy alloy studied by micro- and nanoindentation methods, Acta Mater. 125 (2017) 58–68.
[20] X.Y. Li, K. Lu, Playing with defects in metals, Nat. Mater. 16 (2017) 700–701.
[21] H. Wu, G. Fan, An overview of tailoring strain delocalization for strength–ductility synergy, Prog. Mater. Sci. 113 (2020) 100675.
[22] Y. Wang, M.W. Chen, F.H. Zhou, E. Ma, High tensile ductility in a nanostructured metal, Nature. 419 (2002) 912–915.
[23] W. Sun, Y. Zhu, R. Marceau, L. Wang, Q. Zhang, X. Gao, C. Huthinson, Precipitation strengthening of aluminum alloys by room-temperature cyclic plasticity, Science. 363 (2019) 972–975.
[24] K.S. Ming, W.J. Lu, Z.M. Li, X.F. Bi, J. Wang, Amorphous bands induced by low temperature tension in a non-equiatomic CrMnFeCoNi alloy, Acta Mater. 188 (2020) 354–365.

[25] Y.Q. Wang, B. Liu, K. Yan, M.S. Wang, S. Kabra, Y.L. Chiu, D. Dye, P.D. Lee, Y. Liu, B. Cai, Probing deformation mechanisms of a FeCoCrNi high-entropy alloy at 293 and 77 K using in situ neutron diffraction, Acta Mater. 154 (2018) 79–89.
[26] W.Y. Huo, F. Fang, H. Zhou, Z.H. Xie, J.K. Shang, J.Q. Jiang, Remarkable strength of CoCrFeNi high-entropy alloy wires at cryogenic and elevated temperatures, Scripta Mater. 141 (2017) 125–128.
[27] H.S. Kim, P. Dharmaiah, B. Madavali, R. Ott, K.H. Lee, S.J. Hong, Large-scale production of $(GeTe)_x(AgSbTe2)_{100-x}$(x=75, 80, 85, 90) with enhanced thermoelectric properties via gas-atomization and spark plasma sintering, Acta Mater. 128 (2017) 43–53.
[28] W.Z. Zhai, W.L. Lu, P. Zhang, M.Z. Zhou, X.J. Liu, L.P. Zhou, Microstructure, mechanical and tribological properties of nickel-aluminium bronze alloys developed via gas-atomization and spark plasma sintering, Mater. Sci. Eng. A 707 (2017) 325–336.
[29] W.T. Read, W. Shockley, Dislocation Models of Crystal Grain Boundarm, Phys. Rev. 78 (1950) 275–289.
[30] G. Laplanche, A. Kostka, C. Reinhart, J. Hunfeld, G. Eggeler, E.P. George, Reasons for the superior mechanical properties of medium-entropy CrCoNi compared to high-entropy CrMnFeCoNi, Acta Mater. 128 (2017) 292–303.
[31] I. Moravcik, J. Cizek, Z. Kovacova, J. Nejezchlebova, M. Kitzmantel, E. Neubauer, I. Kubena, V. Hornik, I. Dlouhy, Mechanical and microstructural characterization of powder metallurgy CoCrNi medium entropy alloy, Mater. Sci. Eng. A 701 (2017) 370–380.
[32] B.L. Han, C.C. Zhang, K. Feng, Z.G. Li, X.C. Zhang, Y. Shen, X.D. Wang, H. Kokawa, R.F. Li, Z.Y. Wang, P.K. Chu, Additively manufactured high strength and ductility CrCoNi medium entropy alloy with hierarchical microstructure, Mater. Sci. Eng. A 820 (2021) 141545.
[33] P.D. Niu, R.D. Li, K.F. Gan, T.C. Yuan, S.Y. Xie, C. Chen, Microstructure, Properties, and Metallurgical Defects of an Equimolar CoCrNi Medium Entropy Alloy Additively Manufactured by Selective Laser Melting, Metall. Mater. Trans. A 52A (2021) 753.
[34] N. Hansen, Hall-Petch relation and boundary strengthening, Scripta Mater. 51 (2004) 801–806.
[35] S. Yoshida, T. Bhattacharjee, B. Yu, N. Tsuji, Friction stress and Hall-Petch relationship in CoCrNi equi-atomic medium entropy alloy processed by severe plastic deformation and subsequent annealing, Scripta Mater. 134 (2017) 33–36.
[36] S. Guan, D. Wan, K. Solberg, F. Berto, T. Welo, T.M. Yue, K.C. Chan, Additive manufacturing of fine-grained and dislocation-populated CrMnFeCoNi high entropy alloy by laser engineered net shaping, Mater. Sci. Eng. A 761 (2019) 138056.

[37] M. Zaiser, E.C. Aifantis, Geometrically necessary dislocations and strain gradient plasticity—a dislocation dynamics point of view, Scripta Mater. 48 (2) (2003) 133–139.
[38] M.D. Sangid, T. Ezaz, H. Sehitoglu, I.M. Robertson, Energy of slip transmission and nucleation at grain boundaries, Acta Mater. 59 (2011) 283–296.
[39] Y.L. Zhang, J.G. Li, X.G. Wang, Y.P. Lu, Y.Z. Zhou, X.F. Sun, The interaction and migration of deformation twin in an eutectic high-entropy alloy $AlCoCrFeNi_{2.1}$, J. Mater. Sci. Technol. 35 (2019) 902–906.
[40] J.H. Lee, T.B. Holland, A.K. Mukherjee, X.H. Zhang, H.Y. Wang, Direct observation of Lomer-Cottrell Locks during strain hardening in nanocrystalline nickel by in situ TEM, Sci. Rep. 3 (2013) 1061.
[41] S. Praveen, J.W. Bae, P. Asghari-Rad, J.M. Park, H.S. Kim, Annealing-induced hardening in high-pressure torsion processed CoCrNi medium entropy alloy, Mater. Sci. Eng. A. 734 (2018) 338–340.
[42] X.L. Ma, C.X. Huang, J. Moering, M. Ruppert, H.W. HÖppel, M. GÖken, J. Narayan, Y. Zhu, Mechanical properties of copper/bronze laminates: Role of interfaces, Acta Mater. 116 (2016) 43–52.
[43] S.C. Li, C.Y. Guo, L.L. Hao, Y.L. Kang, Y.G. An, In-situ EBSD study of deformation behaviour of 600 MPa grade dual phase steel during uniaxial tensile tests, Mater. Sci. Eng. A 759 (2019) 624–632.